Supporting Information

Hollow NiO/Carbon Pompon for Efficient Lithium Ions Storage

Ming-Jun Xiao,[a] Bo Ma,[a] Hong Zhang,[b] Xiang-Yang Li,[a] Qiang Wang,*[a] Yong Peng,*[b] and Hao-Li Zhang*[a, c]

a State Key Laboratory of Applied Organic Chemistry, Key Laboratory of Special Function Materials and Structure Design, College of Chemistry and Chemical Engineering, Lanzhou University, Lanzhou, 730000, P. R. China.

b Key Laboratory of Magnetism and Magnetic Materials of MOE, Lanzhou University, Lanzhou, 730000, P. R. China.

c Tianjin Key Laboratory of Molecular Optoelectronic Sciences, Department of Chemistry, Tianjin University, Collaborative Innovation Center of Chemical Science and Engineering (Tianjin), Tianjin 300072, P. R. China.

*Corresponding Author.

E-mail: haoli.zhang@lzu.edu.cn, qiangwang@lzu.edu.cn, pengy@lzu.edu.cn

Materials preparation

The mix 1 g nickel nitrate ($Ni(NO_3)_2 \cdot 6H_2O$) and 6 g of 1-butyl-3-methylimidazole dicyandiamide ($C_8H_{11}N_5$) in 30 ml of ethylene glycol. The mixture was placed in a teflon-lined autoclave, reacted at 160 °C for 10 h, centrifuged to remove the supernatant, and dried at 100 °C for 10 h to obtain hollow pompon-like amorphous nickel carbon composite material (amNiC). Finally, the amNiC was placed in a tube furnace and heated at 320 °C for 1 h in an air atmosphere to obtain NiO/NDC. After heat treatment at 400 °C for 1 h in an air atmosphere, the bare NiO was obtained. Under nitrogen atmosphere, heated at 320 °C for 1 h, the NiO@Ni/NDC was obtained. The heating rate during the heat treatment was 5 °C min^{-1}. By controlling the content of $C_{10}H_{15}N_5$ (1 g, 3 g, 9 g), NiO/NDC with different shapes (hair-ball, yolk-shell pompon-like, irregularity) can be obtained. By controlling the type of IL ($C_8H_{11}N_5$, $C_8H_{15}N_2BF_4$), different morphologies of NiO/NDC (hollow pompon-like, flower-like) can be obtained. By controlling reaction temperature (130 °C, 160 °C, 190 °C) and reaction time (160 °C/5 h, 160 °C/10 h, 160 °C/20 h), different morphology of NiO/NDC (sphere, hollow pompon-like, nanosheet) can be obtained. NDC was obtained by heating $C_{10}H_{15}N_5$ (1 g) in a tube furnace (320 °C for 1 h). Commercial NiO was purchased from Shanghai Macklin Biochemical Co.,Ltd (Metals basis of 99.99%).

Characterization of the samples

X-ray diffraction (XRD) measurements were performed on a Rigaku D/MAX with Cu Ka radiation at a scan rate of 5 min^{-1} and the 2θ range from 10° to 90°. The chemical state of the material surface was analyzed by X-ray photo-electron spectroscopy (XPS) (Kratos Axis Ultra). Transmission electron microscopy (TEM) images, high-resolution transmission electron microcopy (HRTEM) images, high-angle annular dark-field scanning transmission electron microscopy (HAAF-STEM) images, energy dispersive spectroscopy (EDS), and element mappings were obtained on a FEI-Talos200s microscope operating at 200 kV.

Atomic-scale STEM images and aomic-scale element mappings were acquired by probe aberration-corrected STEM (Cubed Titan G2 60-300, FEI, USA) operating voltages of 300 kV. Scanning electron microscope (SEM) images were performed on an Apreo S (Thermo scientific) operating at 20 kV. Raman spectra were obtained with a 633 laser on a confocal microscope Raman system (Renishaw inVia Raman microscope). The Fourier transform infrared spectrum (FTIR) was performed on a Nicolet-670 FTIR spectro-photometer by mixing the sample with KBr and compressing it into a transparent disk. The material specific surface area and pore size distribution were measured with ASAP2020Plus HD88 equipment. Thermo-gravimetric (TG) curve was performed on a thermal analyzer with a heating rate of 5 ^{o}C min^{-1}. The C and N content were measured using elemental analysis (Elementar Analysens systeme GmbH).

In-situ TEM

In-situ TEM experiments were performed on a FEI Talos F200S using a Proto-chips atmosphere (Pfelffer Vacuum D-35614Asslar) sample holder. First, hollow pompon-like amNiC materials were dispersed in deionized water and sonicated. Then, the suspension was pipetted onto the MEMS in-situ heating chip while blowing dry with a dry air ball, and finally the chip was mounted in a Proto-chips atmosphere. To avoid sample contamination, both the chip and the sample holder were plasma cleaned by 30 minutes. The gas environment is to simulate air by passing oxygen (30%) and nitrogen (70%) in the Proto-chips, and heating.

LIBs Performance measurements

The working electrodes were obtained by the samples (70 wt%), carbon black (20 wt%) and polyvinylidene fluoride (PVDF) (10 wt%) in N-methyl-2-pyrrolidone (NMP) and pasting onto pure copper foil, followed in a vacuum oven at 80 ^{o}C for 10 h. The active materials mass loading was about 0.8 mg cm^{-2}. The cells were assembled in an argon filled glove box with a coated copper disk as the working electrode, lithium metal foil as the counter/reference

electrode, and 1 M solution of $LiPF_6$ in a 1:1 (volume ratio) mixture of ethylene carbonate (EC) and diethyl carbonate (DEC) as the electrolyte. Celgard 2400 film was used as a separator film. Charge (lithium insertion) and discharge (lithium extraction) were obtained using coin-cell CR2032 at 30 ^{o}C (refrigerator) between the potentials of 0.01-3.00 V. The cyclic voltammetry (CV) measurement was carried out on a CHI 660E electrochemical workstation at different scan rate (0.2-1.6 mV s^{-1}). The impedance spectra were obtained over the frequency range from 100 kHz to 0.01 Hz. During the galvanostatic intermittent titration technique (GITT) test, the cells were discharged at a constant current density of 0.05 mA under a voltage range of 0.01-3.00 V.

Simulations of atomic resolution STEM images

The atomic-scale STEM images were quantitatively simulated using the quantitative STEM Simulations Package (QSTEM, Arizona State University, USA). The parameters settings of the simulation process are as consistent as possible with the experimental conditions, so the parameters are set as: The high voltage, Cs coefficient, Cc coefficients and defocus were 300 kV, 50 µm, 1.2 mm and 0 nm, respectively. The unit cells of Nx, Ny and Nz were set to be $8 \times 8 \times 10$. The inner angle and outer angle of HAADF detectors were 90 mrad and 170 mrad, respectively. The semi-angle of the incident converged beam was set to 20 mrad. All simulated images use the measured TEM data with the same thickness of 82.7 Å. Thermal Diffuse Scattering (TDS) run was set up 30.

Computational details

All DFT calculations were implemented with the Vienna ab Initio Simulation Package[1]. Pristine carbon was depicted by a $12 \times 12 \times 1$ graphite-type carbon super-cell. The modeled structures were simulated with the generalized gradient approximation with the Perdew-Burke-Ernzerhof functional along with van der Waals interaction by Grimme's D3 scheme[2], which gives good bond lengths and has energy errors that are small compared to the

adsorption errors. For NiO/NDC composite, the dominant phase from surface analysis was the (111) surface; therefore, a (111) surface of bulk NiO was cleaved to make a slab with enough vacuum region, while the $12 \times 12 \times 1$ defected nitrogen doped carbon was placed on it. To avoid spurious interactions between neighboring slabs, we introduce a vacuum of ~ 20 Å, which ensures dispersion forces are sufficiently small on the scale of key energetics. The atoms in the lowest part of the two layers are left untouched, while the atoms in the upper two layers are relaxed during geometric optimization to simulate the active surface. Nudged elastic band (NEB) was employed for studying lithium-atom migration pathway[3]. Lithium carbon adsorption energy (E_{ads}) was calculated as follows:

$$E_{ads} = E_{ad} - E_a - E_b \tag{S1}$$

All energies are Gibbs free energy corrected at room temperature, where the total energy of lithium atom, carbon structure, and interacted structure of carbon and lithium atom are denoted as E_{ad}, E_a, and E_b accordingly.

Equivalent circuit model of Nyquist plots
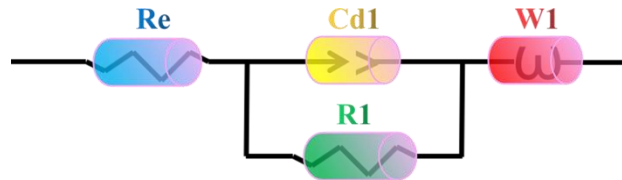
Re represents the intrinsic resistance, *R1* represents the electrode and electrolyte interface charge transfer impedance, *Cdl* denotes the double-layer capacitance, and *W1* denotes the Warburg impedance.

Lithium ion diffusion coefficient (D_{Li+}) calculation

$$D_{Li^+} = \frac{R^2 T^2}{2 A^2 n^4 F^4 C^2 \sigma_w^2} \tag{S2}$$

where R is gas constant, T is the absolute temperature (298 K), A is electrode surface area (A=1.13×10^{-4} m^2), n is the number of electrons transferred (n=8), F is Faraday constant,

5

C is Li$^+$ phase concentration, and σ_w is Warburg coefficient. The σ_w can be obtained by using the following Eq.

$$Z^{'} = R_e + R_{ct} + \sigma_w \omega^{-0.5} \tag{S3}$$

The w is the angular frequency. Thus, σ_w can be acquired by linear fitting Z′ vs. w$^{-0.5}$ the low-frequency range. The calculated lithium diffusion coefficients of hollow pompom NiO/NDC and NiO are shown in the **Table S1** below.

Table S1. Electrochemical impedance spectroscopy fitted results of hollow pompon-like NiO/NDC and NiO.

Sample	Equivalent resistance (Re)	Charge transfer resistance (R1)	Li$^+$ diffusion coefficient (D_{Li+})
NiO/NDC	10.9 Ω	672 Ω	1.13×10^{-18} cm^2 s^{-1}
NiO	11.4 Ω	1109 Ω	1.19×10^{-19} cm^2 s^{-1}
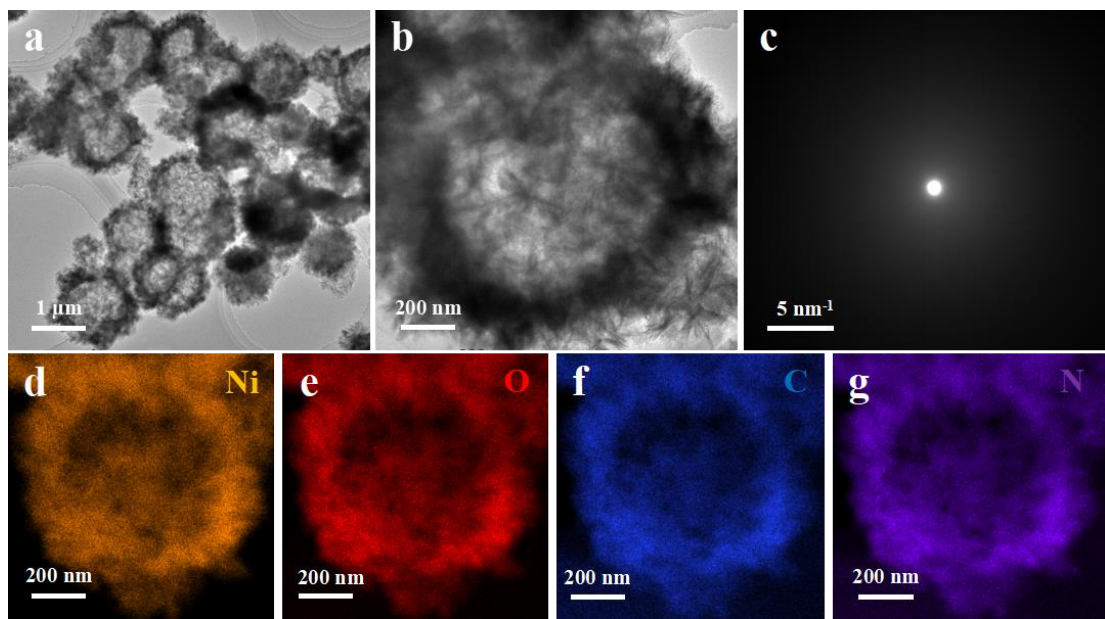
Fig. S1. TEM images (a), a particle TEM image (b), selected area electron diffraction (SAED) pattern (c), and elements mapping (d-g) of hollow pompon-like amNiC.
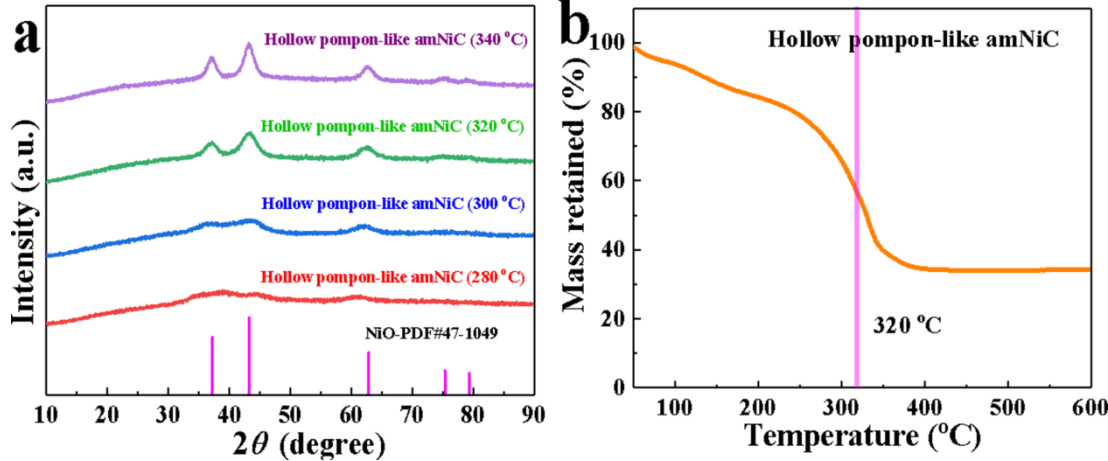

Fig. S2. The XRD (a) of the hollow pompon-like amNiC at different temperatures under air atmosphere. The thermo-gravimetric (TG) curves (b) of the hollow pomon-like amNiC under air atmosphere.
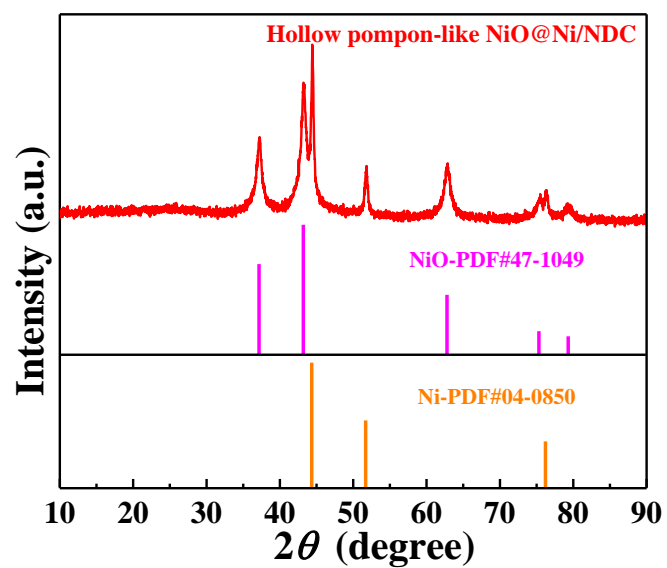
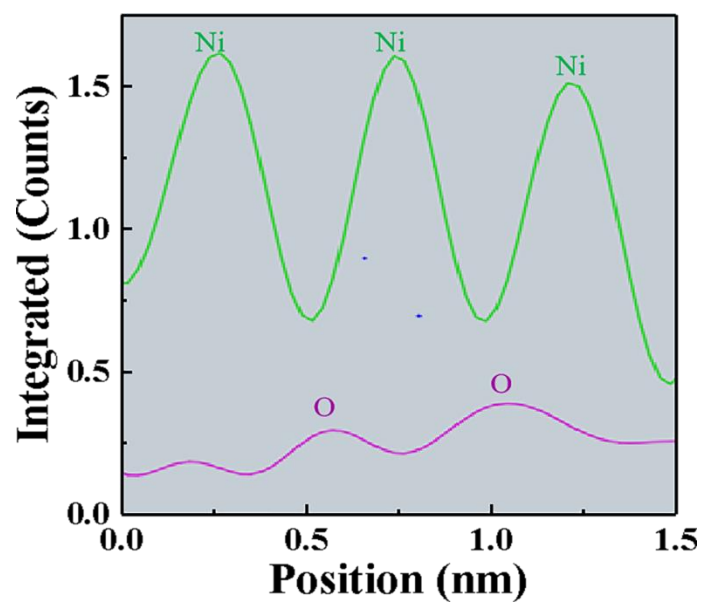**Fig. S3.** The XRD of the hollow pompon-like amNiC at 320 °C under nitrogen atmosphere.

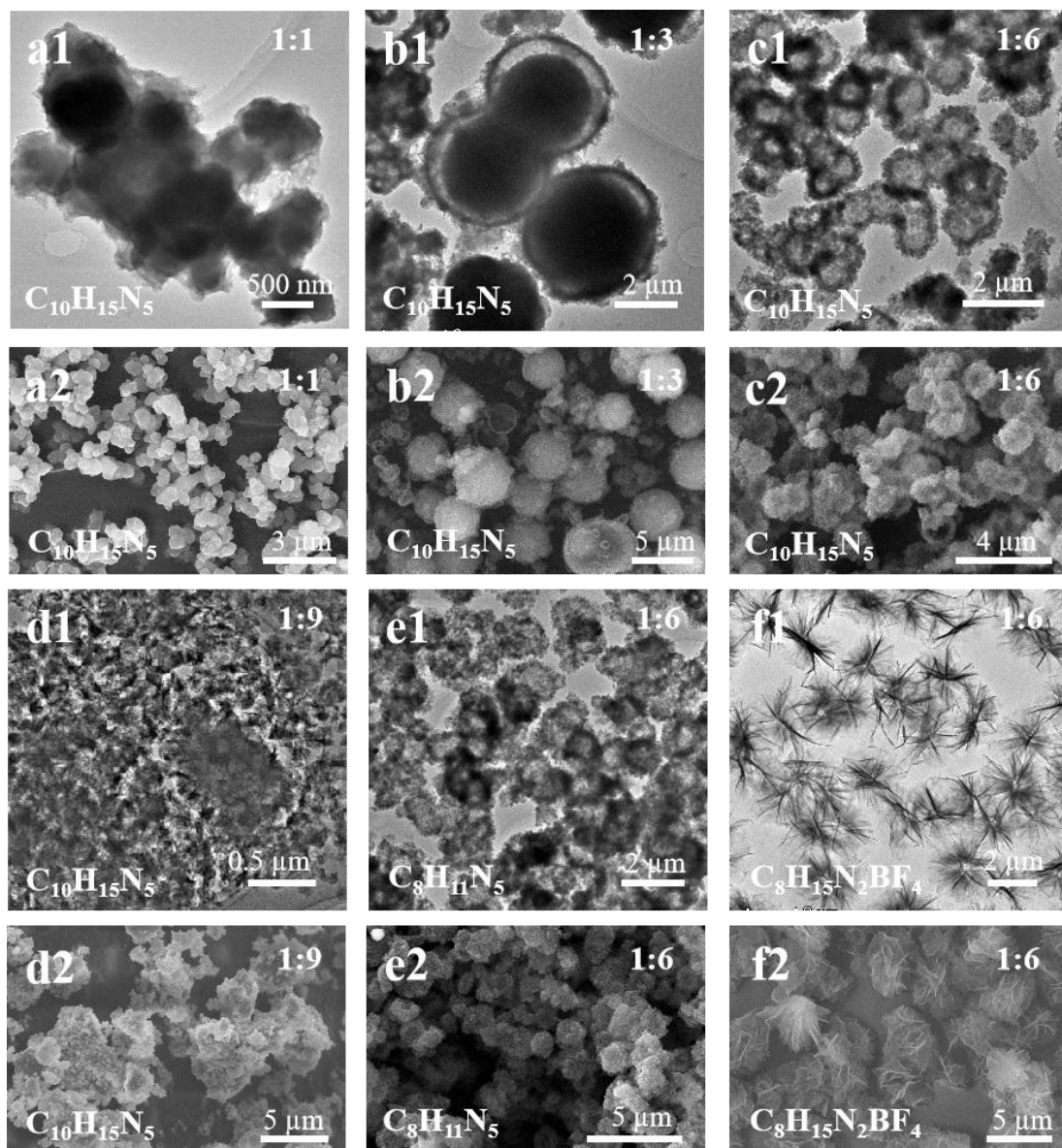**Fig. S4.** The line intensity profiles of atomic in the hollow pompon-like NiO/NDC.

Fig. S5. TEM images (a1-f1) and SEM images (a2-f2) of different morphology amNiC.
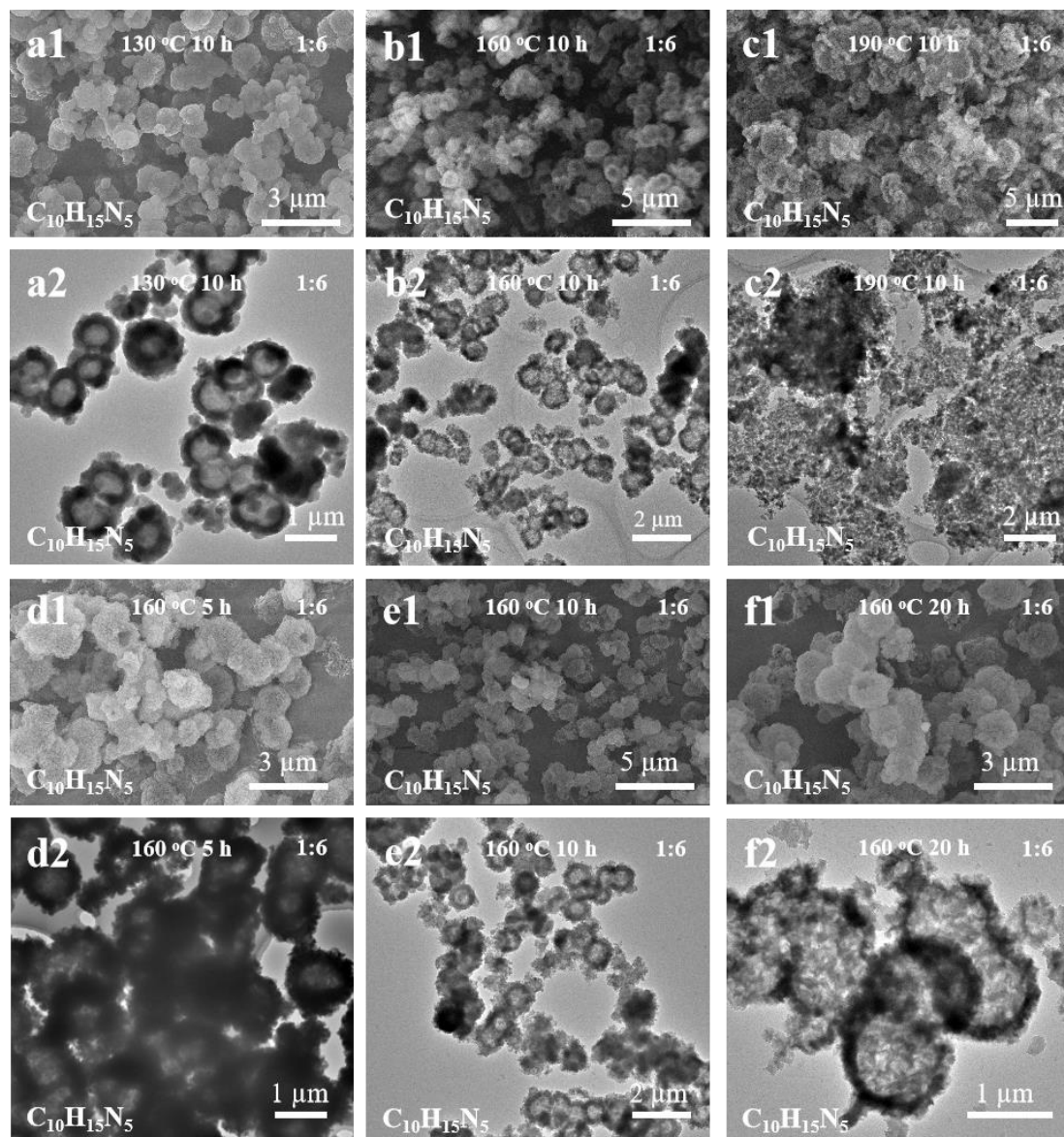
Fig. S6. SEM images (a1-c1) and TEM images (a2-c2) of the amNiC at different reaction temperature in the high-pressure reactor (Ni:IL=1:6); SEM images (d1-f1) and TEM images (d2-f2) of the amNiC at different reaction time at 160 °C in the high-pressure reactor (Ni:IL=1:6).
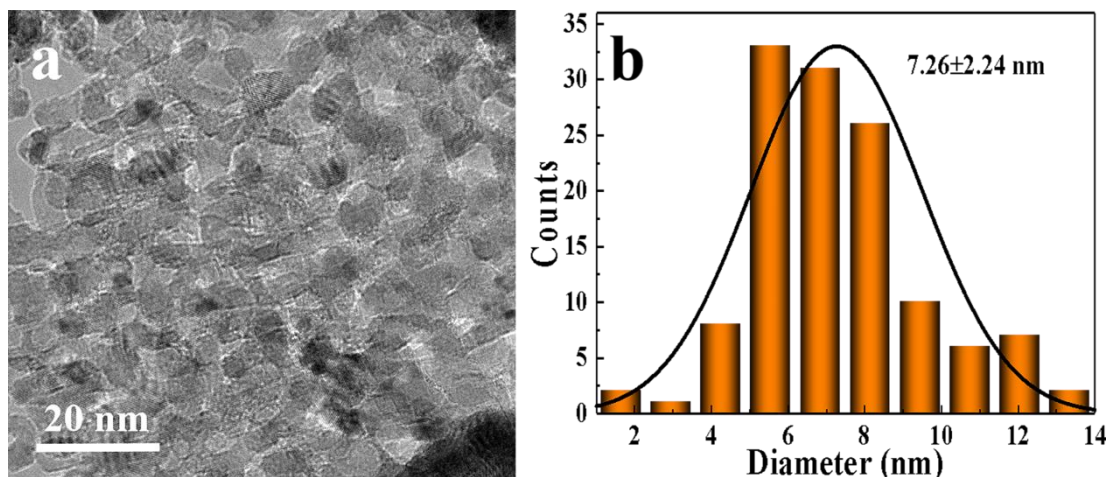
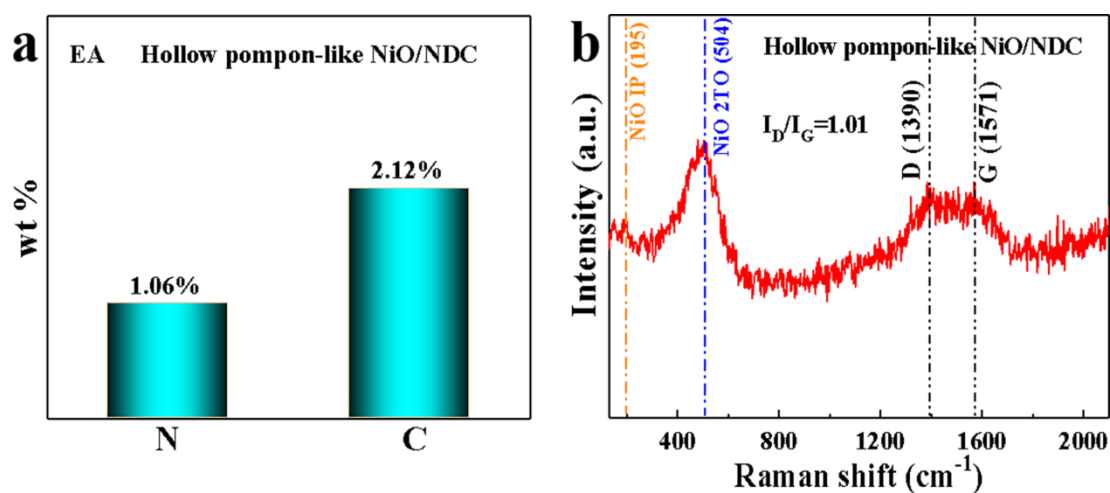**Fig. S7.** TEM image (a) and the corresponding particle size statistics (b) of NiO/NDC.

Fig. S8. The elemental analysis (a) and Raman (b) of hollow pompon-like NiO/NDC.
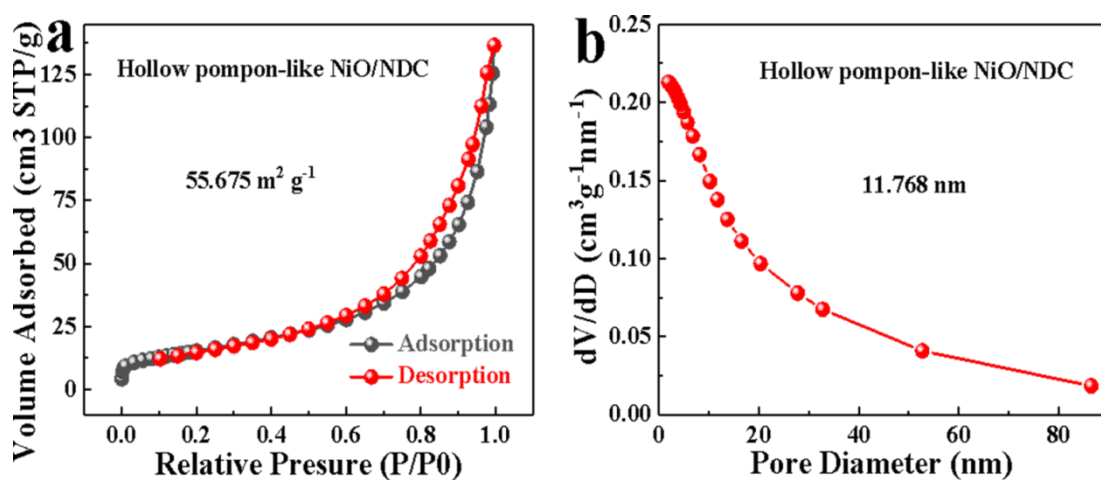

Fig. S9. The nitrogen adsorption/desorption isotherms (a) and the pore size distribution (b) of hollow pompon-like NiO/NDC.
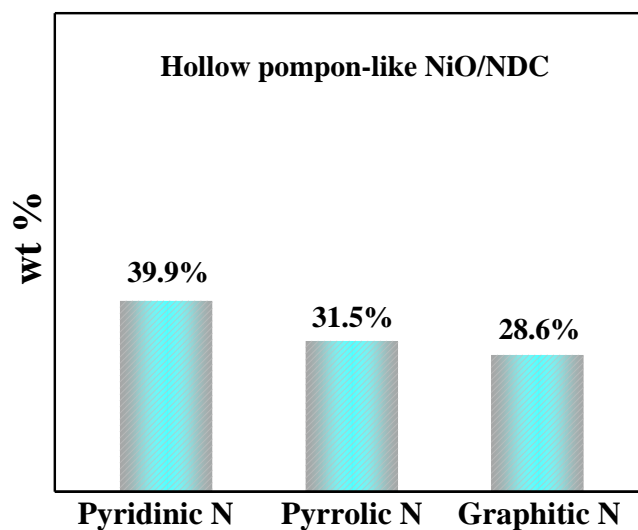
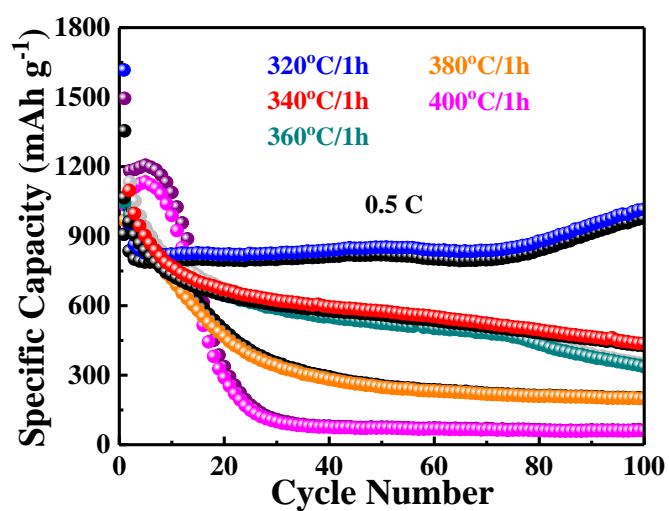**Fig. S10.** The content of different type nitrogen of hollow pompon-like NiO/NDC.

Fig. S11. Cycle performance of the hollow pompon-like NiO/NDC obtained from different heating temperatures.
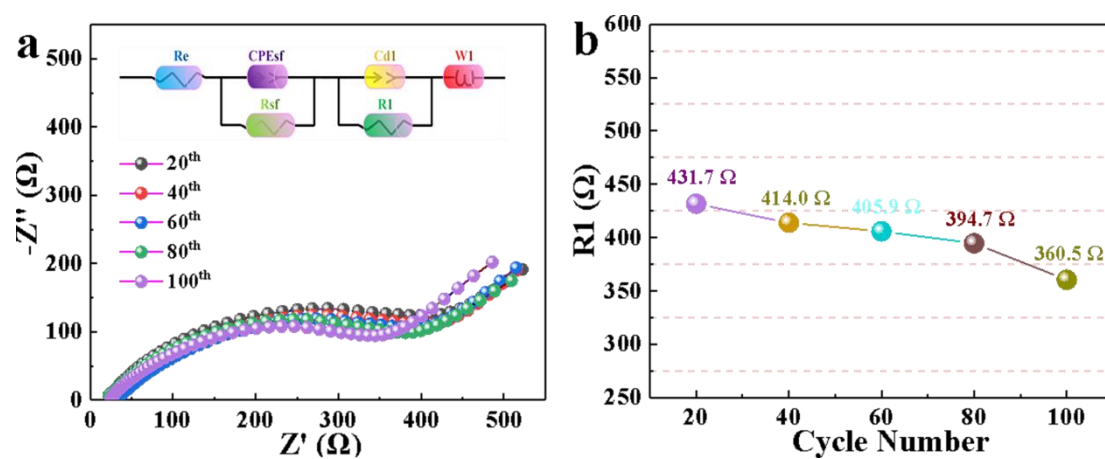
Fig. S12. Nyquist plots and fitted results (inset of the equivalent circuit) (a), charge transfer resistance (b) of hollow pompon-like NiO/NDC.
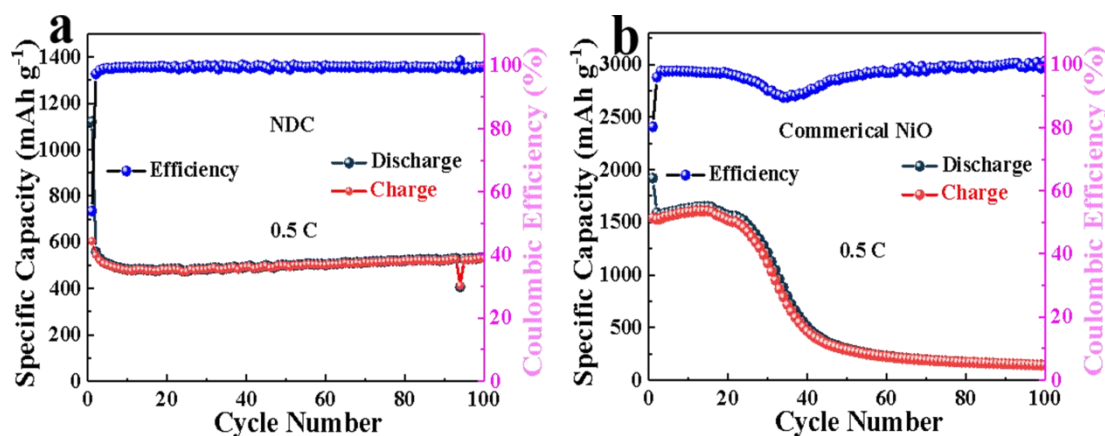

Fig. S13. Cycle performance of NDC (a) and commerical NiO (b) at current density of 0.5 C.
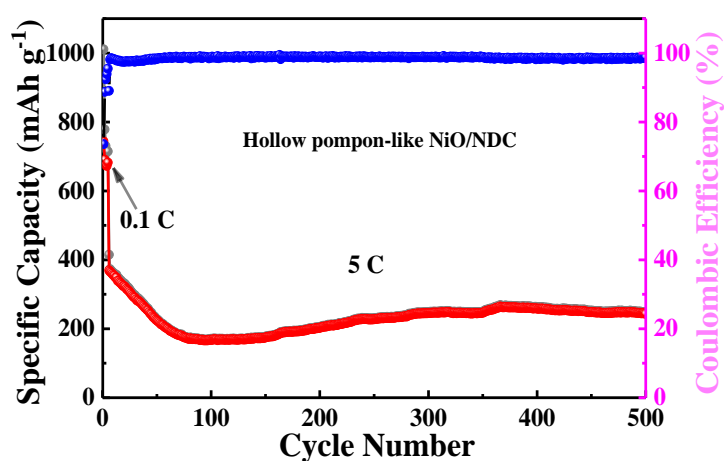

Fig. S14. Cycle performance of hollow pompon-like NiO/NDC at current density of 5 C.
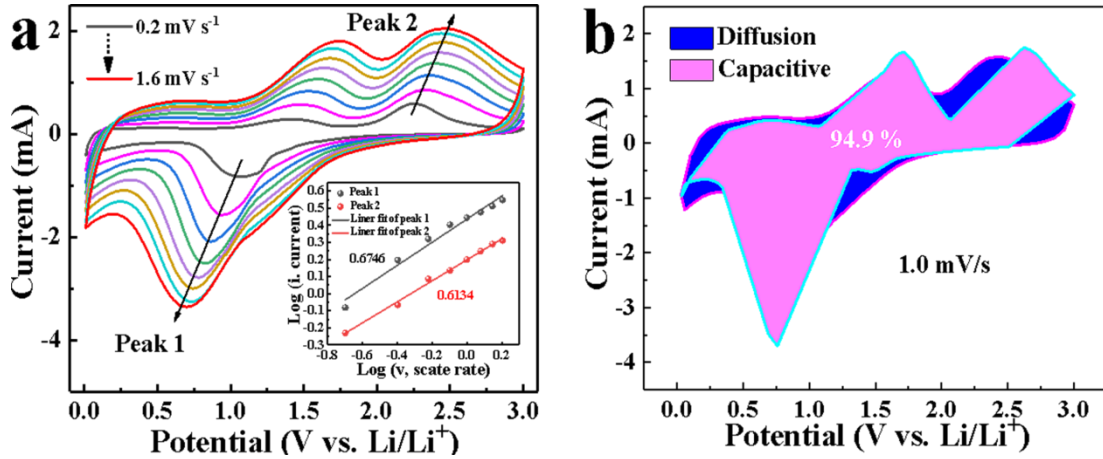
Fig. S15. Cyclic voltammetry (CV) curves (a) at different scan rates (Inset the relationship between peak current and scan rate linear), the capacitive charge and total charge at 1.0 mV s^{-1} (b) of hollow pompon-like NiO/NDC.

The electrochemical performance are influenced by capacitance behavior[4]. To analyze the capacitive behavior of the hollow pompon-like NiO/NDC, CV curves at different scan rates were measured (**Fig. S15a**). The relationship between the peak current (i) and the scan rate (v) is shown by the following Eq.[4, 5].

$$i = av^b \tag{S4}$$

When b=1, it is capacitive behavior control. When b=0.5, it is mainly diffusion control[6]. By plotting, the b values of the cathodic and anodic peaks are obtained to be 0.6746 and 0.6134, respectively (**Fig. S15a**, inset part), indicating that the material has capacitive behavior and diffusion process. The value for the capacitive contribution (k_1v) and diffusion contribution ($k_2v^{0.5}$) are derived from the following Eq.[6].

$$i = k_1v + k_2v^{0.5} \tag{S5}$$

Therefore, at a scan rate of 1 mV s^{-1}, the capacitive behavior of hollow pompon-like NiO/NDC accounts for about 94.9% (**Fig. S15b**).
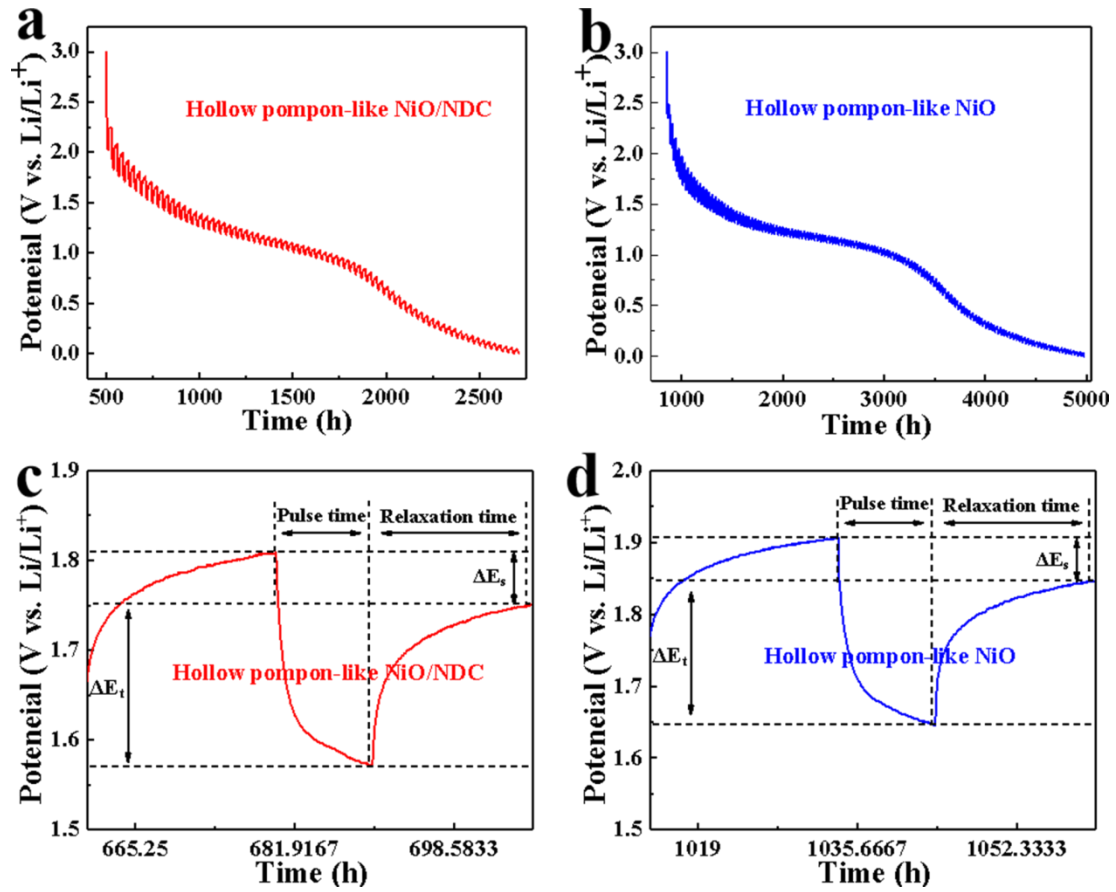
14

Fig. S16. Galvanostatic intermittent titration technique curves of hollow pompon-like NiO/NDC (a) and NiO (b); A single titration with the galvanostatic intermittent titration technique of hollow pompon-like NiO/NDC(c) and NiO (d).

Galvanostatic intermittent titration technique (GITT) measurements were used to measure the diffusion process of lithium ion during the galvanostatic discharge processes at 0.5 C (**Fig. S16a, b**). In addition, the diffusion coefficient of lithium ion (D_{Li+}) can be quantitatively calculated by Eq.[7]: $D_{Li^+} = \dfrac{4}{\pi\tau} \times (\dfrac{m_B V_M}{M_B S})^2 \times (\dfrac{\Delta E_S}{\Delta E_t})^2$. Where m_B and M_B are the active mass and molar mass, V_M is the molar volume, S is the active area of the electrodes, τ is the pulse time, and ΔE_s and ΔE_t are the pulse time and the voltage difference during discharge and charge, as shown in **Fig. S16c, d**.
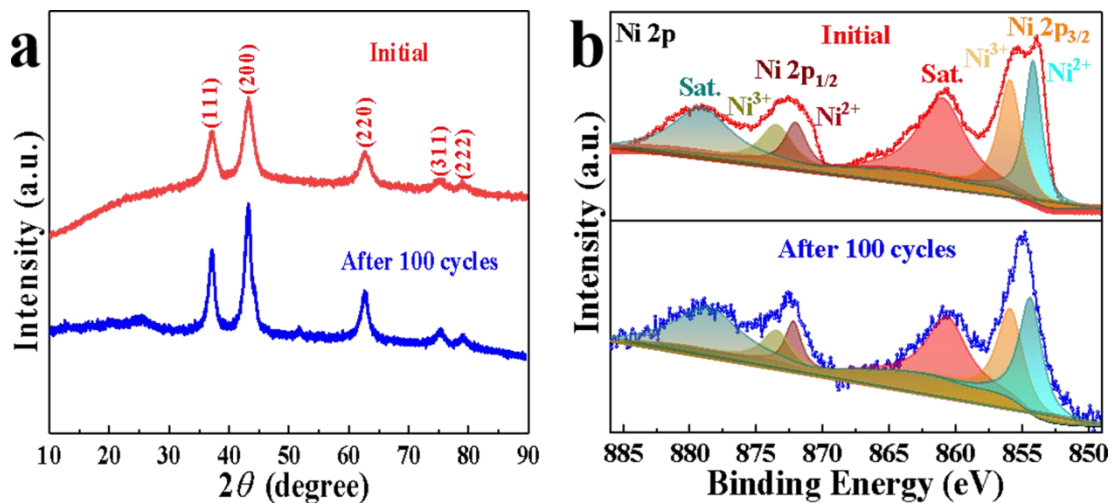
Fig. S17. XRD pattern (a) and high-resolution XPS of Ni 2p spectra (b) of hollow pompon-like NiO/NDC initial and after 100 cycles at current density of 0.5 C.

Table S2. The data of Ni 2p XPS of hollow pompon-like NiO/NDC initial and after 100 cycles.

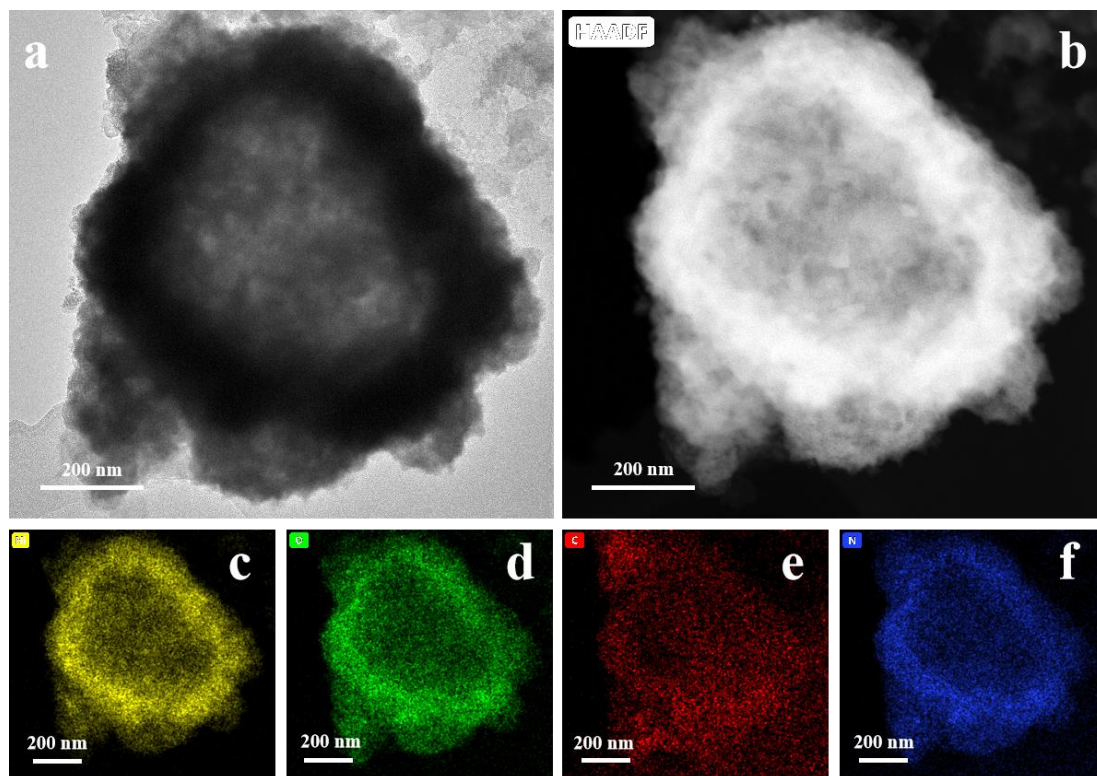| Ni 2p (Initial NiO/NDC)			Ni 2p (After cycle NiO/NDC)		
Peak	Binding Energy	Content	Peak	Binding Energy	Content
Ni^{2+} (Ni 2p$_{3/2}$)	854.1 eV	17.99%	Ni^{2+} (Ni 2p$_{3/2}$)	854.3 eV	19.00%
Ni^{3+} (Ni 2p$_{3/2}$)	855.8 eV	19.10%	Ni^{3+} (Ni 2p$_{3/2}$)	855.8 eV	19.76%
Sat.	860.9 eV	28.10%	Sat.	860.6 eV	24.63%
Ni^{2+} (Ni 2p$_{1/2}$)	871.9 eV	6.98%	Ni^{2+} (Ni 2p$_{1/2}$)	872.1 eV	6.30%
Ni^{3+} (Ni 2p$_{1/2}$)	873.4 eV	8.61%	Ni^{3+} (Ni 2p$_{1/2}$)	873.4 eV	7.52%
Sat.	879.0 eV	19.22%	Sat.	878.5 eV	22.79%

16

Fig. S18. TEM image (a), HAADF-STEM image (b) and element mapping (c-f) of hollow pompon-like NiO/NDC after 100 cycles at current density of 0.5 C.

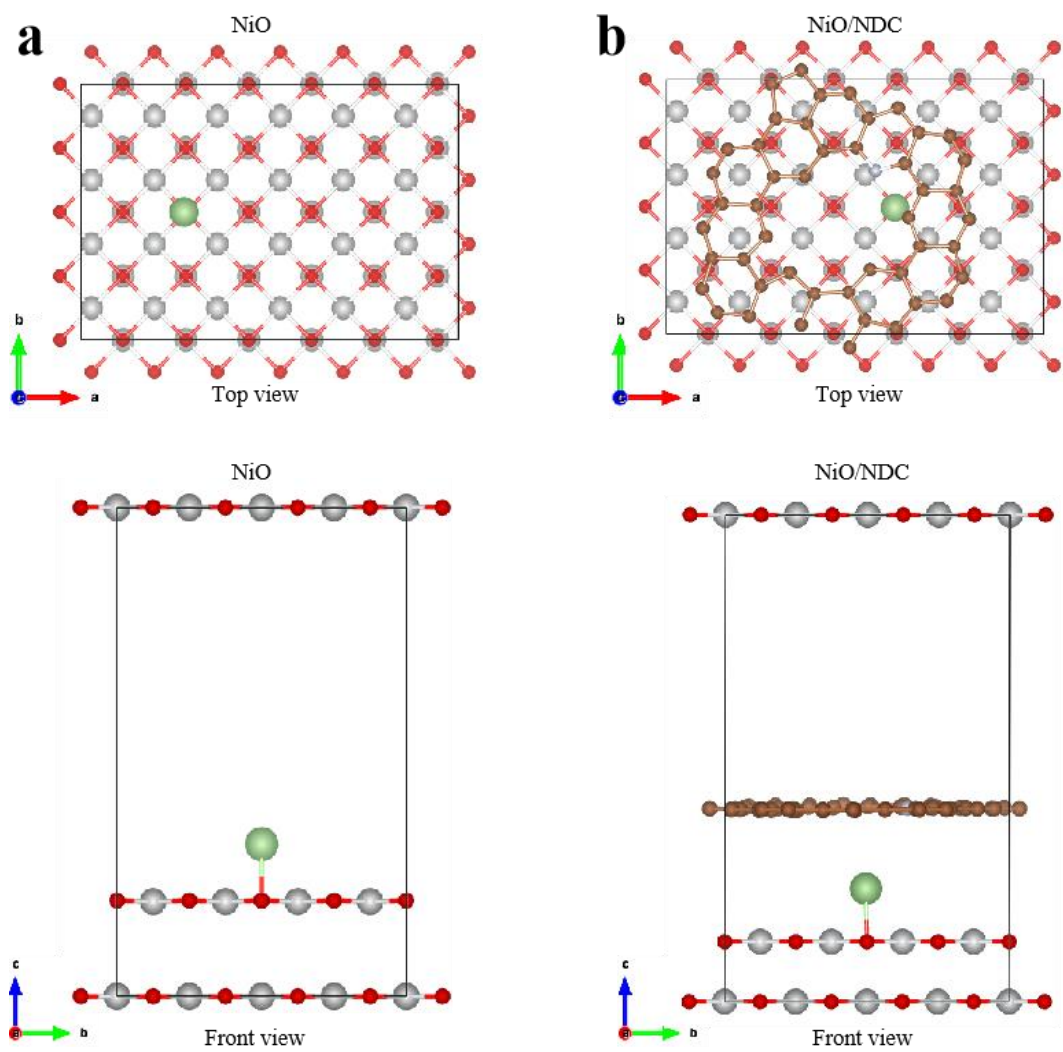**Fig. S19.** SEM image of hollow pompon-like NiO/NDC after 100 cycles at current density of 0.5 C.

Fig. S20. The models of NiO super cell (a) and NiO/NDC super cell (b).

Table S3. Charge transfer data of C and NDC (C1, C2, and C3 are the three C atoms around N1. Original charge is the original valence electron of ZAV in POTCAR. Final charge is the valence electron from ACF. Charge transfer is final original).

	C1	C2	C3	N1
C (Original charge)	4 e	4 e	4 e	0 e
C (Final charge)	4 e	4 e	4 e	0 e
C (Charge transfer)	0 e	0 e	0 e	0 e
NDC (Original charge)	4 e	4 e	0 e	5 e
NDC (Final charge)	3.65 e	3.6 e	0 e	6.1 e
NDC (Charge transfer)	-0.35 e	-0.4 e	0 e	1.1 e

Table S4. Adsorption energy for the NiO, NDC, and NiO/NDC systems.

	NiO	NDC	NiO/NDC	
Slab	-22.76452 eV	-591.46533 eV	-795.19876 eV	-2.08562 eV
Abs+Li	-24.85013 eV	-603.12134 eV	-797.28438 eV	-0.32317 eV
Abs	-1.76245 eV	-11.33284 eV	-796.96121 eV	-603.12134 eV
	-1.76245 eV	-9.57039 eV	-2.08562 eV	

Table S5. Diffusion energy of lithium diffusion for the NiO and NiO/NDC systems.

NiO	0	1.9641	1.0695	1.6031	2.457	2.7244	0.1542
NiO/NDC	0	1.0175	0.8038	0.8507	0.8093	0.8156	0.0105

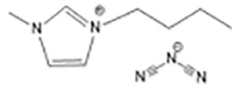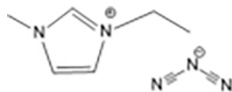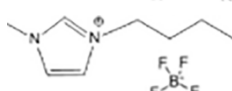**Table S6.** The full names and molecular structures of the three ILs are listed.

Full names	Molecular formula	Structure formula	Molecular weight
1-butyl-3-methylimidazolium dicyanamide	$C_{10}H_{15}N_5$		220
1-ethyl-3-methylimidazolium dicyanamide	$C_8H_{11}N_5$		188
1-butyl-3-methylimidazolium tetrafuoroborate	$C_8H_{11}N_2BF_4$		226

Table S7. The electrochemical performance comparison of NiO-based anode materials for LIBs.

Materials	Method	Specific capacity	References
Core-shell ultrathin NiO nanosheets grown on hollow carbon microspheres	Precipitation method followed by an annealing	992 mA h g^{-1} after 100 cycles of 0.5 A g^{-1}	[8]
Anchoring NiO nanosheets on flat carbon hollow particles	Precipitation reaction and followed by annealing	950 mA h g^{-1} after 150 cycles of 0.2 A g^{-1}	[9]
Porous NiO microspheres intercon-nected by carbon nanotubes	Pyrolysis of nickel metal organic framework precursors	812 mA h g^{-1} after 100 cycles of 0.1 A g^{-1}	[10]
NiO-graphene hybrid	Liquid phase deposition method	646 mA h g^{-1} after 35 cycles of 100 mA g^{-1}	[11]
Ultrathin graphite/carbon nanotube/NiO composite	Chemical vapor deposition and subsequent electrodeposition	995 mA h g^{-1} after 100 cycles of 200 mA g^{-1}	[12]

Ultrathin porous NiO nanosheets/graphene	Hydrothermal methods	1098 mA h g^{-1} after 50 cycles of 100 mA g^{-1}	[13]
Oxygen bridges between NiO nanosheets and graphene	Hydrothermal reaction and annealed	883 mA h g^{-1} after 50 cycles of 50 mA g^{-1}	[14]
Carbon-encapsulated NiO nanoparticles on porous reduced grapheme oxide matrix	Annealing process using Ni(OH)$_2$/RGO hybrid aerogel	1003 mA h g^{-1} after 1000 cycles of 200 mA g^{-1}	[15]
Stacked NiO nanosheets@carbon and ultrathin NiO nanosheets@functionalized carbon	One-pot reaction and topotactic conversion	1113 mA h g^{-1} after 800 cycles of 1000 mA g^{-1}	[16]
Coral-like yolk-shell-structured nickel oxide/carbon composite microspheres	Spray pyrolysis	991 mA h g^{-1} after 500 cycles of 1 A g^{-1}	[17]
Porous NiO/C composites	Hydrothermal reaction and calcination	727 mA h g^{-1} after 150 cycles of 100 mA g^{-1}	[18]
Multifunctional carbon encapsulated Ni@NiO nanocomposites	Hydrothermal reaction and annealed	975 mA h g^{-1} after 400 cycles of 200 mA g^{-1}	[19]
Hollow pompon-like NiO/NDC	Solvothermal method and low temperature heat treatment	1014 mA h g^{-1} after 100 cycles of 0.5 C	This work

To provide an overall picture, we have compared the pompon-like hollow NiO/NDC hybrid materials prepared with this new method with the previously reported NiO-based nanomaterials in **Table S7**. It can be seen that the reversible capacity of hollow NiO/Carbon pompon composition prepared in this work over performs the most reported NiO-based nanomaterials under similar condition. It is believed that this ionic liquid based synthetic method can become a very competitive method to fabricate hierarchical NiO carbon composite for LIB applications.

Reference

1. G. Kresse and G. Kresse, *Phys. Rev. B*, 1996, **54**, 11169.

2. John, P., Perdew, Kieron, Burke, Matthias and Ernzerhof, *Phys. Rev. Lett.*, 1997, **78**, 1396.

3. G. Henkelman and H. JoóNsson, *J. Chem. Phys.*, 2000, **113**, 9978-9985.

4. Q. Long, W. M. Chen, Z. H. Wang, Q. G. Shao, X. Li, L. X. Yuan, X. L. Hu, W. X. Zhang and Y. H. Huang, *Adv. Mater.*, 2012, **24**, 2047-2050.

5. S. Lu, T. Zhu, Z. Li, Y. Pang, L. Shi, S. Ding and G. Gao, *J. Mater. Chem. A*, 2018, **6**, 7005-7013.

6. Z. Hu, L. Wang, K. Zhang, J. Wang, F. Cheng, Z. Tao and J. Chen, *Angew. Chem., Int. Ed*, 2014, **53**, 12794-12798.

7. J. Jiang, Y. Zhang, Y. An, L. Wu, Q. Zhu, H. Dou and X. Zhang, *Small Methods*, 2019, **3**, 1900081-1900090.

8. B. Wang, G. Wang, X. Cheng and H. Wang, *Chem. Eng. J.*, 2016, **306**, 1193-1202.

9. J. Liang, H. Hu, H. Park, C. Xiao, S. Ding, U. Paik and X. W. Lou, *Energy Environ. Sci.*, 2015, **8**, 1707-1711.

10. Y. Xu, S. Hou, G. Yang, T. Lu and L. Pan, *J. Solid State Electrochem.*, 2017, **22**, 785-795.

11. Y. J. Mai, S. J. Shi, D. Zhang, Y. Lu, C. D. Gu and J. P. Tu, *J. Power Sources*, 2012, **204**, 155-161.

12. W. Liu, C. Lu, X. Wang, K. Liang and B. K. Tay, *J. Mater. Chem. A*, 2015, **3**, 624-633.

13. Y. Huang, X. L. Huang, J. S. Lian, D. Xu, L. M. Wang and X. B. Zhang, *J. Mater. Chem.*, 2012, **22**, 2844-2844.

14. G. M. Zhou, D. W. Wang, L. C. Yin, N. Li, F. Li and H. M. Cheng, *ACS Nano*, 2012, **6**, 3214-3223.

15. C. Ding, W. Zhou, X. Wang, B. Shi, D. Wang, P. Zhou and G. Wen, *Chem. Eng. J.*, 2018, **332**, 479-485.

16. J. Zhang, W. Luo, T. Xiong, R. Yu, P. Wu, J. Zhu, Y. Dai and L. Mai, *Nanoscale*, 2019, **11**, 7588-7594.

17. M. S. Jo, S. Ghosh, S. M. Jeong, Y. C. Kang and J. S. Cho, *Nano-Micro Lett.*, 2019, **11**. https://doi.org/10.1007/s40820-018-0234-0.

18. Y. Tan, Q. Li, Z. Lu, C. Yang, W. Qian and F. Yu, *J. Alloys Compd.*, 2021, **874**, 159788-159788.

19. D. Xu, C. Mu, B. Wang, J. Xiang, W. Ruan, F. Wen, X. Du, Z. Liu and Y. Tian, *Sci. China Mater.*, 2017, **60**, 947-954.